

1                   **A bedform phase diagram for dense granular currents**

2   <sup>1</sup>Gregory Smith\*, <sup>1,2,3</sup> Peter Rowley, <sup>1</sup>Rebecca Williams, <sup>4</sup>Guido Giordano, <sup>4</sup>Matteo Trolese,  
3   <sup>4</sup>Aurora Silleni, <sup>5</sup>Daniel R. Parsons, <sup>2</sup>Samuel Capon

4   <sup>1</sup>*Department of Geography, Geology and Environment, University of Hull, Hull, UK*

5   <sup>2</sup>*School of Earth and Environmental Sciences, University of Portsmouth, Portsmouth, UK*

6   <sup>3</sup>*Department of Geography and Environmental Sciences, University of the West of England,*  
7   *Bristol, UK*

8   <sup>4</sup>*Dipartimento di Scienze, Università Roma Tre, Roma, Italia*

9   <sup>5</sup>*Energy and Environment Institute, University of Hull, Hull, UK*

10

11   \**Gregory.Smith-2016@hull.ac.uk*

12

13                   **This paper is a peer-reviewed preprint submitted to EarthArXiv**

14

15

16

17

18

19

20

21

22

23

24

## A bedform phase diagram for dense granular currents

25

26 **Pyroclastic density currents are a life-threatening volcanic hazard. Our understanding**  
27 **and hazard assessments of these flows rely on interpretations of their deposits. The**  
28 **occurrence of stratified layers, cross-stratification, and bedforms in these deposits has**  
29 **been assumed as indicative of dilute, turbulent, supercritical flows causing traction-**  
30 **dominated deposition. Here we show, through analogue experiments, that a variety of**  
31 **bedforms can be produced by denser, aerated, granular currents, including backset**  
32 **bedforms that are formed in waning flows by an upstream-propagating granular bore.**  
33 **We are able to, for the first time, define phase fields for the formation of bedforms in**  
34 **PDC deposits. We examine how our findings impact the understanding of bedform**  
35 **features in outcrop, using the example of the Pozzolane Rosse ignimbrite of the Colli**  
36 **Albani volcano, Italy, and thus highlight that interpretations of the formative**  
37 **mechanisms of these features observed in the field must be reconsidered.**

38

## 39 INTRODUCTION

40 Particulate density currents are the largest mass transporters of sediment on the Earth's  
41 surface. Deep-sea turbidity currents deposit the largest sediment accumulations on Earth<sup>1</sup>,  
42 density currents emplace ejecta blankets around bolide impact craters<sup>2</sup> and pyroclastic density  
43 currents (PDCs) can transport thousands of cubic kilometres of volcanic material during a  
44 single event<sup>3</sup>. These flows also pose a major geohazard, with deep-sea turbidity currents  
45 threatening seafloor infrastructure and PDCs being responsible for over 90,000 deaths since  
46 1600 CE<sup>4,5</sup>. Understanding the behaviour of these particle-laden, fast-moving currents is  
47 fundamental to decreasing the risks they pose to society.

48 The dynamics and depositional processes of PDCs are difficult to analyse due to their  
49 destructiveness, and the concealment of the internal dynamics by an accompanying ash cloud.  
50 Understanding of PDC behaviour therefore, is primarily based on interpretation of the  
51 geological record preserved in sedimentary deposits<sup>6-10</sup>, complemented by analogue and  
52 numerical modelling<sup>11-14</sup>.

53 The presence and morphology of sedimentary structures, such as bedforms, in a deposit can  
54 be interpreted to tell us about the internal behaviour of the density current that formed them<sup>15-</sup>  
55 <sup>19</sup>. Various types of cross-stratified bedforms occur in PDC strata and are assumed to be  
56 formed by dilute, high-velocity (surge) PDCs<sup>8,18,20-24</sup>, where tractional processes dominate in  
57 the flow-boundary zone due to the predominance of fluid turbulence as a particle support  
58 mechanism<sup>9,11,25,26</sup>. Denser, granular fluid-based PDCs are usually thought to be responsible  
59 for the creation of massive deposits, lacking in sedimentary structures<sup>6,9,27,28</sup>.

60 Bedform-related sedimentary structures in PDC deposits include backset features (i.e.  
61 upstream-dipping beds) formed by stoss-side aggradation, similar to chute-and-pool  
62 structures and antidunes found in fluvial systems (Fig. 1a & 1f and Fig. 1b & 1d), which are  
63 generally thought to be formed under supercritical flow conditions<sup>16,19,29,30</sup>. Early work on  
64 such structures in PDC deposits interpreted them similarly as the result of supercritical  
65 flows<sup>31-34</sup>. These backset bedforms have commonly been referred to as 'regressive', for  
66 example by Allen<sup>18</sup> who interpreted them as 'sandwaves' deposited by wet and cool  
67 pyroclastic surges. Since then 'regressive' has been commonly used to describe stoss-  
68 aggrading features in PDC deposits, although linking this to flow conditions, rather than  
69 temperature and moisture content<sup>21, 35-37</sup>. However, there have been attempts to introduce  
70 new terminology which does not hold the genetic connotations of 'antidune', 'chute-and-  
71 pool', or 'sandwave'. For example, Brown and Branney<sup>38</sup> use 'regressive bed form' for a  
72 giant set of sigmoidal, upstream dipping lenses. Douillet et al.<sup>22</sup> introduce the term

73 ‘regressive climbing dunes’ for bedforms which show upstream crest migration (Fig. 1c).  
74 Brand et al.<sup>39</sup> adopt similar terminology, using ‘regressive dune bedforms’ (Fig. 1e). In this  
75 paper we avoid using such terms, in the interests of being purely descriptive, opting instead to  
76 use ‘backset bedforms’ to refer to stoss-aggrading features which have both asymmetrical  
77 (much steeper stoss sides; Fig. 1g) or roughly symmetrical lee and stoss slopes (Fig. 1h).

78 Analogue modelling of dense PDCs has advanced considerably over recent years including  
79 work focusing on the influence of pore pressure<sup>13,40-45</sup>. High gas pore pressure created by  
80 various mechanisms within PDCs<sup>6,9,46-48</sup> has been shown to be responsible for their unusually  
81 high mobility<sup>49-51</sup>, but only recently has physical modelling reflected the sustained and  
82 variable nature of such pore pressures with distance from source<sup>44,52</sup>.

83 Here we examine the conditions which promote the growth of bedforms in aerated dense  
84 granular flows, as analogues for PDCs and their deposits. This work describes laboratory  
85 experiments in which we use partially fluidised (“aerated”) fine-grained particles in a 3 m  
86 long flume (see Methods). These experiments are able to simulate many behaviours of  
87 PDCs<sup>13,43,44,52</sup>. As the deposit aggrades from the quasi-steady currents, the growth of  
88 bedforms is recorded using a high-speed camera. We study how backset bedform features  
89 form within the dense granular currents. Deposition is triggered in the experiments as the  
90 sustained aerated flow passes into a section of the flume with a reduced or absent basal gas  
91 flux, resulting in rapid deaeration and a consequent increase in frictional forces between  
92 particles. This is not intended to represent a specific natural process but rather simulate the  
93 rapid deaeration hypothesised to occur in natural PDCs as a result of various processes such  
94 as loss of fines, temperature drops, thinning, and/or the entrainment of coarser material<sup>45,48,53</sup>.  
95 The initial deaeration would be accelerated by the slowing current (decreasing shear rates),  
96 and increasing inter-particle frictional forces. We are able to, for the first time, define phase  
97 fields for the formation of types of bedforms in PDC deposits using current velocity, current

98 thickness, Froude number, and Friction number. We examine how our interpretations impact  
 99 on the understanding of similar features in outcrop, using the example of the Pozzolane Rosse  
 100 ignimbrite of the Colli Albani volcano, Italy.

## 101 **RESULTS**

### 102 **Bedform morphology**

103 A range of bedforms were observed growing under a variety of flow conditions within the  
 104 suite of experimental runs (see Methods). We categorise these bedforms into three types (Fig.  
 105 2): i) planar/very shallow backset ( $<2^\circ$ ) bedsets, ii) backset bedforms with shallow stoss sides  
 106 less than the dynamic angle of repose ( $< \theta_{dyn}$ ), and iii) backset bedforms with steep  
 107 ( $>\theta_{dyn}$ ) stoss sides. Planar bedsets, shallow backset bedforms and steep backset bedforms  
 108 are present in each deposit except one (Fig. 2e), which does not show steep backset bedforms.  
 109 Both steep and shallow backset bedforms comprise a bedset of multiple (3-4) stoss-side  
 110 lamina dipping at varying angles, converging into a single corresponding lee-side lamina  
 111 (Table 1). No progressive (prograding) bedforms were observed in any of the experimental  
 112 runs because our experiments are run with waning, not waxing currents.

113 Table 1. Dimensions and angles of our experimental backset bedforms

Bedform	Lengths (m)	Thickness (m)	Stoss angles ( $^\circ$ )	Lee angles ( $^\circ$ )
Steep backset (Fig. 1g)	0.18-0.4	0.35-0.4	20 - overturned	$<10$
Shallow backset (Fig. 1h)	0.18-0.21	0.003-0.01	$<10$	$<10$

114

115

## 116 **Bedform deposition**

117 The experiments began when the particles were released into the flume via trapdoor and  
118 impinged on the basal porous mesh, forming an aerated current. The leading edges of the  
119 currents were travelling at  $\sim 2 \text{ ms}^{-1}$  as they passed into the lesser/un-aerated second chamber  
120 of the flume (Fig. 3a, see Supplementary Movie 1). The sustained currents rapidly deaerate as  
121 they pass over the second chamber of the flume, promoting deposition. Small spontaneously-  
122 generated variations in the current mass flux result in minor unsteadiness in the flow over  
123 timescales in the order of 0.05 s and flow thickness variations in the order of  $\pm 10\%$ , hence  
124 their quasi or nearly-steady nature<sup>44</sup>. The currents initially deposit planar or very shallow  
125 backset bedsets after the break in aeration, (Fig. 3b) at velocities of  $\sim 1\text{-}1.5 \text{ ms}^{-1}$ . Within 0.4-  
126 0.8 s of deposition beginning, stoss-side aggrading shallow backset bedforms are deposited  
127 above and upstream of the planar bedsets as the current velocities decrease (Fig. 3c-d).  
128 Within 1.1-1.6 s of deposition beginning, with the current velocities below  $\sim 0.5 \text{ ms}^{-1}$ , the  
129 upstream edge of the deposit steepens and collapses, with very steep backset bedsets  
130 deposited just prior to this, forming the stoss sides of steep backset bedforms (Fig. 3e-f).  
131 Current velocity and thickness data during deposition of the bedforms may be found in  
132 Supplementary Table 1.

## 133 **Velocity and thickness control on bedform formation**

134 Planar, shallow, and steep features fall into well-defined fields on a current velocity vs  
135 current thickness plot, suggesting that current velocity and thickness controls the sedimentary  
136 structures in the deposit (Fig. 4a). For a given current thickness planar bedsets are deposited  
137 at higher velocities (above  $0.8 \text{ ms}^{-1}$  in these experiments). Shallow backset bedforms are  
138 deposited at lower velocities, and steep backset bedforms are deposited at the lowest  
139 velocities (between  $0.3\text{-}0.6 \text{ ms}^{-1}$  in these experiments). With increasing current thickness,

140 higher current velocities are required to remain in the shallow bedform and planar bedform  
 141 stability fields. As a result of thickening within a steady current, bedform-induced deposits of  
 142 different character can be formed without a requirement for a change in flow velocity. It is  
 143 important to note that the deposit formed over the smallest aeration drop ( $0.66 U_{mf}$  to  $0.53$   
 144  $U_{mf}$ .) does not show steep backset bedforms, and only poorly developed shallow backset  
 145 bedforms, suggesting the magnitude of the aeration drop and consequent velocity changes  
 146 may also have some control.

### 147 **Phase fields**

148 We define phase fields for the three types of bedforms using the Froude number ( $Fr$ ) and the  
 149 Friction Number ( $N_F$ ). The Froude number ( $Fr$ ) represents the ratio of kinetic to potential  
 150 energy (Eq 1).

$$151 \quad Fr = U/(gH)^{1/2} \quad (\text{Eq 1})$$

152 Where  $U$  = current velocity,  $g$  = gravity, and  $H$  = current thickness. The Friction  
 153 Number ( $N_F$ ) is the ratio of frictional to viscous stresses and is defined as Bagnold  
 154 Number/Savage Number<sup>54,55</sup>. The Savage number ( $N_S$ , Eq. 2) is the ratio of collisional stress  
 155 to frictional stress<sup>55,56</sup>, and the Bagnold number ( $N_B$ , Eq. 3) is the ratio of collisional stress to  
 156 viscous fluid stress<sup>55,57</sup>.

$$157 \quad N_S = \frac{\left(\frac{U}{H}\right)^2 \delta^2 \rho_s}{(\rho_s - \rho_f) g H \tan \theta} \quad (\text{Eq 2})$$

$$158 \quad N_B = \frac{\left(\frac{U}{H}\right) \delta^2 \rho_s \varphi}{(1 - \varphi) \mu} \quad (\text{Eq 3})$$

159 where  $\rho_s$  = particle density       $\rho_f$  = fluid density       $\delta$  = particle diameter       $\theta$  =  
 160 internal friction angle       $\varphi$  = solid volume fraction       $\mu$  = fluid viscosity.

161  $N_S$  in these experiments range from 0.00003-0.03, and  $N_B$  from 15-269. In natural PDCs,  $N_S$   
162 has been estimated to range from  $10^{-8}$ - $10^{-9}$ <sup>13</sup>, which similar to our experiments is in the  
163 frictional regime<sup>56</sup> despite the difference of several orders of magnitude. Our  $N_B$  values  
164 overlap with those estimated for natural PDCs ( $10^0$ - $10^2$ )<sup>13</sup>.

165 Froude numbers were calculated for each tracked sediment package during its deposition.  
166 Different types of bedforms are formed under different ranges of  $Fr$ , with greater overlap  
167 between the planar bedset and shallow backset bedform fields than between the shallow and  
168 steep backset bedform fields (Fig. 4b-c). As anticipated, there is a good correlation ( $R =$   
169 0.843) between  $Fr$  and velocity (Fig. 4c), but with a noticeably greater data spread at higher  
170 ( $>0.8 \text{ ms}^{-1}$ ) velocities, whereas  $H$  exerts much less of a control on  $Fr$  (Fig. 4b).

171 Planar bedsets are mostly deposited at high  $Fr$  and low  $N_F$ , shallow backset bedforms at  
172 moderate  $Fr$  and  $N_F$ , and steep backset bedforms at low  $Fr$  and high  $N_F$  (Fig. 4d). The  
173 planar-shallow-steep sequence of bedform formation can therefore be seen as recording the  
174 transition of a fast, supercritical current dominated by viscous stresses to a slower current  
175 increasingly dominated by frictional stresses.

### 176 **Similar bedforms in the field**

177 The Pozzolane Rosse (PR) ignimbrite covers an area of more than 1600 km<sup>2</sup> around the Colli  
178 Albani volcano, Italy<sup>58</sup>, and has been dated (<sup>40</sup>Ar/<sup>39</sup>Ar) at  $456 \pm 3 \text{ ka}$ <sup>59</sup>. It surmounts  
179 topography of 250 m to reach altitudes of 440 m<sup>60</sup>. The ignimbrite is generally massive,  
180 matrix-supported and poorly-sorted, with a noticeable paucity in fine ash. Emplacement  
181 temperatures have been estimated to be between 630 °C and 710 °C<sup>61</sup>.

182 Six samples were taken for this study from three localities (within 18-24 km of the vent; Fig  
183 5a) and two facies (massive, and ‘undulated’ bedding as described in Giordano &  
184 Doronzo<sup>62</sup>). Grains are dominantly poorly vesicular scoria with compositions plotting in the



185 tephrite/basanite field<sup>63</sup>. The grain size distribution of all samples is dominated by lapilli-  
186 sized grains and poor in the < 63  $\mu\text{m}$  fraction (Fig. 5b, Supplementary Table 2), which is  
187 consistent with samples from other studies (Fig. 5c), plotting in the ‘fines-depleted flow’ field  
188 of Walker<sup>25</sup>. Therefore, we consider the parent PDC of the PR ignimbrite to be a good natural  
189 example of an analogue dense, granular current.

190 Rotating drum tests on the six samples taken from the PR (excluding grains > 0.0056 m) gave  
191 static minimum ( $\Theta_{Smin}$ ), maximum ( $\Theta_{Smax}$ ) and dynamic ( $\Theta_{Dyn}$ ) angles of repose of 35.3°,  
192 51.7° and 45.2° respectively (Supplementary Figure 1). Although these values are  
193 considerably higher than those obtained for the particles used in the experiments  
194 (Supplementary Figure 2), (likely due to the variable grainsize and angularity of the  
195 ignimbrite grains), the scaling remains reasonable due to the larger particle sizes in the  
196 natural materials (see Eq. 2).

197 Backset bedforms are found in the ‘undulated bedding’ facies in the NE sector of the PR  
198 ignimbrite, where the depositing current left the radial plain and ran up into the Apennine  
199 mountains<sup>62</sup>. The undulated facies transitions laterally into the massive facies of the PR on  
200 scales of hundreds of metres, and both facies have the same grain size and compositional  
201 characteristics (Fig. 5b-c), thus we interpret them to be from the same parent PDC. The  
202 bedforms in the PR share similarities with our experimental deposits (c.f. Fig. 6a and Fig. 2a-  
203 c, Fig. 6c and Fig. 2d); and measured stoss angles for both natural and experimental bedforms  
204 span the same range (Fig. 6b). The stoss layers seen in the PR backset bedforms are never  
205 overturned upstream like some of the experimental deposits. Preservation of overturned beds  
206 in natural deposits may be difficult – upstream avalanching of material from this unstable  
207 bedform may be reincorporated into a sustained current, or they may be cryptic and not easily  
208 visible in natural material. Shallow stoss-sided bedforms are found in this facies (Fig. 6d)

209 although they tend to have greater lee (due to the greater repose angles of the material) and  
210 stoss angles than experimental examples, where both are  $<10^\circ$  (Fig 6b).

## 211 **DISCUSSION**

212 Our experimental deposits consist of planar bedsets and shallow and steep backset bedforms.  
213 The existing widespread interpretation of backset features in PDC deposits is that they are a  
214 product of upper flow regime/Froude supercritical flow within dilute PDCs<sup>31-35, 64</sup>, or that  
215 relatively steep backset bedforms are specifically a record of the formation and propagation  
216 of Froude jumps, where flow transforms from Froude supercritical ( $>1$ ) to Froude subcritical,  
217 similar to fluvial chute-and-pool structures<sup>20,31,35,37,39,64-66</sup> (Fig. 1a/1e and 1f). Our  
218 experimental currents show rapidly evolving Froude numbers (Fig. 4). Within the current  
219 body, planar beds are deposited at  $Fr$  3-5, shallow backset bedforms at  $Fr$  2-3, and steep  
220 backset bedforms at  $Fr$  0.59-2. We show that an apparent Froude jump within the flow forms  
221 in the current during deposition of the steep backset bedforms (Fig. 7). As the experimental  
222 current is granular, we adopt the term granular jump<sup>67-69</sup>, which shares many characteristics  
223 with its hydraulic counterpart. However, the outgoing current only briefly has  $Fr < 1$ , due to  
224 thickening of the current directly prior to its being blocked, meaning that a granular jump,  
225 strictly defined as a flow transitioning from  $Fr > 1$  to  $Fr < 1$ , exists here for only 0.1 - 0.2  
226 seconds.

227 As the sediment deposit grows in thickness, a critical point is reached where the incoming  
228 flow cannot surpass the negative slope, and the pseudo-jump propagates upstream as a  
229 granular bore<sup>68</sup>, which travels at  $0.14 \text{ ms}^{-1}$  between 96 cm and 90 cm along the flume length.  
230 Here we use ‘granular bore’ to describe the upstream propagation of the depositional front of  
231 the granular material, regardless of flow conditions. This process appears to be similar to the  
232 “stoss-side blocking” or “granular jamming” invoked to explain stoss-aggrading bedforms at

233 Tungurahua<sup>22,70</sup>, where the granular current is simply blocked by topography with no  
234 particular fluid conditions necessary.

235 An interesting feature seen in the granular jump of Boudet et al.<sup>67</sup> and our own currents is the  
236 steepening of stoss faces well beyond the repose angle at the front of the granular bore, and  
237 its collapse by avalanching (Fig. 7d). This is likely caused by rapid deposition from the  
238 incoming flow countering the effects of gravity sliding, and allowing the bedforms to steepen  
239 well beyond repose angle. Again, a similar phenomenon of very high sedimentation rates is  
240 used to explain near-vertical bedding at Tungurahua<sup>70</sup>. The particles deposited by the current  
241 as the deposit front steepens form our steep backset bedforms, with stoss angles up to 90°.  
242 This may explain why the smallest aeration drop in our experiments ( $0.66 U_{mf}$  to  $0.53 U_{mf}$ )  
243 did not form steep backset bedforms – the drop was too small to promote the levels of  
244 deaeration and deceleration necessary for such rapid sedimentation. Our experimental data  
245 therefore call the widespread interpretation of backset bedforms recording Froude jumps  
246 within dilute PDCs into question, as we show that similar features can form in dense granular  
247 flows in relation to an extremely transient Froude jump, and more clearly related to stoss-side  
248 blocking.

249 Calculated  $N_S$  and  $N_B$  numbers indicate that planar bedsets are deposited under conditions  
250 closer to a collision-dominated flow regime ( $N_S > 0.1$  and  $N_B > 450^{71}$ ) than the backset  
251 bedforms (Supplementary Table 1). The planar bedset deposition occurs beyond the transition  
252 to the unfluidised section of flume, and therefore they are deposited by a current which is  
253 experiencing more collisions between particles due to the loss of gas pore pressure. The  
254 backset bedforms are deposited closer to this transition point, where the current has a higher  
255 gas pore pressure and grain collisions are not as prevalent. A ratio of  $N_B$  to  $N_S$  ( $N_F$ ) shows that  
256 frictional stresses are considerably higher than viscous shear stresses in the area of the  
257 currents depositing steep backset bedforms (Fig. 4d). As the current is waning at this point

258 and relatively thick, this could result in sustained contacts between particles despite relatively  
259 high gas pore pressures.

260 The PR ignimbrite is generally massive and fines poor, which suggests that the flow-  
261 boundary zone conditions of the parent PDC were highly concentrated, likely close to the  
262 fluid escape-dominated and granular flow-dominated end-members of Branney and  
263 Kokelaar<sup>9</sup>. Additionally, the dense nature of the clasts, lack of fines and the lack of  
264 widespread stratification all suggest that the ignimbrite is the deposit of a dense, granular  
265 PDC. The presence of backset bedforms within the deposit, which are typically indicative of  
266 dilute, turbulent flow (“pyroclastic surges”), is therefore paradoxical. Rather, the backset  
267 bedforms must have been produced by some other process than turbulence within a dilute  
268 current.

269 The similarities between the structures in the PR ignimbrite and our experimental deposits  
270 formed by a dense granular current suggest that the depositional processes involved in both  
271 cases could be related. We interpret the undulated bedding facies - which includes the backset  
272 bedforms - to have been deposited by the same PDC as the rest of the PR ignimbrite. This is  
273 due to the traceable lateral transition between facies, the similarity between the grain size  
274 curves over a range of localities, and because the tephra is compositionally identical in the  
275 two lithofacies. Instead, the change in facies could be due to the onset of rapid deposition and  
276 stoss-side blocking related to the run-up of the PDC into the Apennine mountains (Fig. 5a).  
277 Giordano & Doronzo<sup>62</sup> interpret the undulated bedding to the east of the volcano as the result  
278 of rapid sedimentation and a reduction in the lateral mass discharge rate caused by a  
279 palaeovalley perpendicular to flow. Our experimental steep stoss-sided bedforms are created  
280 in a waning flow regime after the cessation of basal gas injection and the resulting decrease in  
281 pore pressure results in rapid sedimentation, so these interpretations are consistent.

282 We propose a depositional model whereby shallow backset bedforms are deposited by  
283 supercritical flow, forming a topographic irregularity which slows the incoming current (Fig.  
284 8a-b), causing stoss-side blocking, forming a granular bore and promoting rapid deposition  
285 (Fig. 8c). Continued deposition steepens the front of the bore until it collapses upstream  
286 through avalanching (Fig. 8d-e). Our work provides direct evidence that bedforms can be  
287 created by dense granular PDCs, and supports the stoss-side blocking process first suggested  
288 by Douillet<sup>22,70</sup> based on field deposits.

289 The upstream propagation of a granular bore, which is caused by the blocking of the current  
290 by the aggrading deposit, is a process which in nature could be exacerbated or triggered by  
291 pre-existing topography<sup>69</sup>. The waning nature of the incoming flow at this point, and its  
292 relatively low Froude number, suggests that while most of these steep backset bedforms are  
293 technically recording the transition from supercritical to subcritical flow, both the shallow  
294 backset bedforms and planar beds are formed under increasingly supercritical conditions. It  
295 follows that shallow backset bedforms and planar bedsets may then be better indicators of  
296 supercritical flow conditions when interpreting dense PDC deposits. The proposed phase  
297 diagrams presented here are a major step towards quantitative links between PDC processes  
298 and their deposits.

299 Bedforms can be the product of a dense granular flow and can form without any interference  
300 (e.g. tractional shear) from an overlying dilute turbulent layer. As the presence of bedforms  
301 (e.g. cross-stratification and backsets) has been commonly used as diagnostic evidence for  
302 dilute, turbulent currents, our findings have important implications for field interpretation –  
303 as different types of PDCs can react differently to topography the correct classification is  
304 necessary for hazard assessment. Other sedimentary characteristics such as field relations,  
305 grain size and sorting must be used in order to distinguish between the two PDC end-  
306 members. This challenge to the interpretation of the deposits of particulate granular currents

307 is particularly relevant to other free-surface granular mass flows, including landslides, snow  
308 avalanches, and debris flows. Our experiments demonstrate that formation of different  
309 bedforms may be controlled by current thickness and current velocity which has important  
310 implications for hazard mapping, and the potential for further investigation to a) expand the  
311 bedform stability criteria identified here, and b) define palaeoflow conditions from recorded  
312 bedforms.

## 313 **METHODS**

### 314 **Flume set-up**

315 We use the experimental flume of Smith et al.<sup>52</sup>, modified so that release of the particulate  
316 density current is controlled by a trapdoor instead of a horizontal lock gate (Fig. 9), such that  
317 colour stratification in the starting charge transmits to the flow and deposit. The base of the  
318 flume comprises one-meter long sections which can provide independently controlled gas  
319 fluxes through a porous baseplate in each section in order to fluidise any overpassing  
320 material. The flume was kept at an angle of  $2^\circ$ , to promote flow away from the impingement  
321 surface while maintaining a sub-horizontal surface.

322 The air-supply plumbing allows a gas flux to be fed through the base of the flume, producing  
323 sustained aeration of the current. In such thin ( $<0.03$  m), rapidly degassing laboratory  
324 currents, this enables us to simulate the long-lived high gas pore pressures that characterize  
325 thicker PDCs<sup>44,52</sup>. The gas flux supplied through the base in each of the three sections of the  
326 channel was controlled to vary the aeration state of the currents, all of which were below  
327 minimum fluidisation velocity ( $U_{mf}$ ), as complete fluidisation would result in non-  
328 deposition<sup>44</sup>.

329 Various aeration states were used to trigger different flow behaviours. The first chamber  
330 ( $0.66$ - $0.93 U_{mf}$ ) always had higher gas flux than the second chamber ( $0$ - $0.66 U_{mf}$ ) to trigger

331 deposition in the target area of the flume. The experiments were recorded using a high-speed  
332 camera at 200 frames per second. This video recorded a side-wall area of the channel at 1 m  
333 runout (across the contact between the first and second gas supply chambers), allowing for  
334 measurement of the flow conditions. From the opening of the trapdoor to the cessation of  
335 deposition each experimental run lasted approximately four seconds.

### 336 **Experimental material and deposits**

337 The experiments were performed using particles of spherical soda lime ballotini with grain  
338 sizes of 45-90  $\mu\text{m}$  (average  $D_{32} = 63.4 \mu\text{m}$  calculated from six samples across the material  
339 batch) similar to the particles used in previous experimental granular currents<sup>40,42,44</sup>. These  
340 ballotini belong to the Group A classification of Geldart<sup>72</sup>, comprising particles 45-90  $\mu\text{m}$   
341 which expand homogeneously above  $U_{mf}$  until bubbles form, and which are non-cohesive. As  
342 PDCs contain dominantly Group A particles, this allows dynamic similarity between the  
343 natural and experimental currents<sup>13</sup>. Detailed mechanical properties of the ballotini are  
344 presented in Supplementary Table 3, derived from rotating drum<sup>73</sup> and shearbox (BS 1377-  
345 7:1990) testing. These give cohesion values of 0 kPa, and an internal friction angle of  $25.3^\circ$   
346 (Supplementary Figure 3). Static minimum ( $\Theta_{smin}$ ), maximum ( $\Theta_{smax}$ ) and dynamic ( $\Theta_{Dyn}$ )  
347 angles of repose are found to be of  $11.7^\circ$ ,  $31.9^\circ$  and  $20.9^\circ$  respectively (Supplementary  
348 Figure 2).

349 Due to the monodisperse nature of the materials, any internal structure is easily masked by  
350 lack of contrast between packages of sediment<sup>74</sup>. To this end the charge for each experiment  
351 was built up of layers of dyed beads so that flow packages could be tracked throughout flow  
352 and deposition, as used in Rowley et al.<sup>44</sup>. Reported velocities are calculated by tracking  
353 these coloured sediment packages in the body of the current immediately prior to their  
354 deposition.

355 When reporting the length of a bedform, the distance from the onset of the stoss-side lamina  
356 to the termination of the lee slope on the depositional surface was measured. Thickness refers  
357 to the distance between the lowest point of a lamina in the bedform to the highest point of a  
358 lamina in that same bedform (Fig. 1g and 1h). Bedform lengths and thicknesses are reported,  
359 as opposed to wavelengths and amplitudes, as we do not produce repetitive trains of  
360 bedforms. This is because of the short nature of the experiments – the current is not sustained  
361 for long enough, and doing so would require an unfeasible amount of material under the  
362 current set-up.

### 363 **Error measurements**

364 Errors (2 s.d.) for various measurements are as follows: current thickness:  $\pm 0.0013$  m. Current  
365 velocity:  $\pm 0.055$  ms<sup>-1</sup>.  $Fr$ :  $\pm 0.17$ .  $N_F$ :  $\pm 67,000$ .

### 366 **DATA AVAILABILITY**

367 Data supporting the graphs in Fig. 4 is derived from raw video files and is available in  
368 Supplementary Table 1. One experimental run is available as Supplementary Movie 1. Four  
369 other videos, are available upon reasonable request.

### 370 **REFERENCES**

- 371 1: Bouma, A. H., Normark, W. R. & Barnes, N. E. Submarine Fans and Related Turbidite  
372 Systems. *Frontiers in Sedimentary Geology* (Springer, New York, NY, 1985).
- 373 2: Siegert, S., Branney, M. J. & Hecht, L. Density current origin of a melt-bearing impact  
374 ejecta blanket. *Geology* **45**, 855-858 (2017).
- 375 3: Self, S. The effects and consequences of very large explosive volcanic eruptions. *Philos. T.*  
376 *R. Soc. A* **364** (2006).



- 377 4: Auker, M. R., Sparks, R. S. J., Siebert, L., Crossweller, H. S. & Ewert, J. A statistical analysis  
378 of the global historical volcanic fatalities record. *J. Appl. Volcanol.* **2** (2013).
- 379 5: Tanguy, J.-C., Ribière, Ch., Scarth, A. & Tjetjep, W. Victims from volcanic eruptions: a  
380 revised database. *Bull. Volcanol.* **60**, 137-144 (1998).
- 381 6: Sparks, R. S. J. Grain size variations in ignimbrites and implications for the transport of  
382 pyroclastic flows. *Sedimentology* **23**, 147–188 (1976).
- 383 7: Wilson, C. J. N. The Taupo eruption, New Zealand: II. The Taupo Ignimbrite. *Philos. T. R.*  
384 *Soc. A* **314**, 229-310 (1985).
- 385 8: Cas, R. A. F. & Wright, J. V. Volcanic Successions: Modern and Ancient (Allen and  
386 Unwin, London, 1987).
- 387 9: Branney, M. J. & Kokelaar, P. Pyroclastic density currents and the sedimentation of  
388 ignimbrites. *Geol. Soc. London. Memoir* **27** (2002).
- 389 10: Pollock, N. M., Brand, B. D., Rowley, P. J., Sarocchi, D., Sulpizio, R. Inferring  
390 pyroclastic density current flow conditions using syn-depositional sedimentary structures.  
391 *Bull. Volcanol.* **81**,46 (2019).
- 392 11: Valentine, G. A. Stratified flow in pyroclastic surges. *Bull. Volcanol.* **49**, 616-630 (1987).
- 393 12: Dobran, F., Neri, A. & Macedonio, G. Numerical simulation of collapsing volcanic  
394 columns. *J. Geophys. Res.* **98**, 4231-4259 (1993).
- 395 13: Roche, O. Depositional processes and gas pore pressure in pyroclastic flows: An  
396 experimental perspective. *Bull. Volcanol.* **74**, 1807–1820 (2012).
- 397 14: Dufek, J. The fluid mechanics of pyroclastic density currents. *Annu. Rev. Fluid. Mech.*  
398 **48**, 459-485 (2016).

- 399 15: Bouma, A. H. *Sedimentology of Some Flysch Deposits* (Elsevier, Amsterdam, 1962).
- 400 16: Jopling, A. V. & Richardson, E. V. Backset bedding developed in shooting flow in  
401 laboratory experiments. *J. Sed. Petrol.* **36**, 821-825 (1966).
- 402 17: Normark, W. R., Hess, G. R., Stow, D. A. V. & Bowen, A. J. Sediment waves on the  
403 Monterey Fan levee: A preliminary physical interpretation. *Mar. Geol.* **37**, 1-18 (1980).
- 404 18: Allen, J. *Sedimentary Structures: Their Character and Physical Basis, Volume 2.* (Elsevier,  
405 Amsterdam, 1982).
- 406 19: Alexander, J., Bridge, J. S., Cheel, R. J. & Leclair, S. F. Bedforms and associated  
407 sedimentary structures formed under water flows over aggrading sand beds. *Sedimentology* **48**,  
408 133-152 (2001).
- 409 20: Schmincke, H.-U., Fisher, R. V. & Waters, A. C. Antidune and chute and pool structures  
410 in the base surge deposits of the Laacher See area, Germany. *Sedimentology* **20**, 553-574  
411 (1973).
- 412 21: Cole, P. Migration direction of sand-wave structures in pyroclastic-surge deposits:  
413 implications for depositional processes. *Geology* **19**, 1108-1111 (1991)
- 414 22: Douillet, G. A. et al. Dune bedforms produced by dilute pyroclastic density currents from  
415 the August 2006 eruption of Tungurahua volcano, Ecuador. *Bull. Volcanol.* **75**, 762 (2013).
- 416 23: Wohletz, K. H. & Sheridan, M. F. A model of pyroclastic surge. *Geol. Soc. Am. Sp. Pap.*  
417 **180**, 177–194 (1979).
- 418 24: Walker, G. P. L. Characteristics of dune-bedded pyroclastic surge bedsets. *J. Volcanol.*  
419 *Geotherm. Res.* **20**, 281–296 (1984).
- 420 25: Walker, G. P. L. Ignimbrite types and ignimbrite problems. *J. Volcano. Geotherm. Res.* **17**,  
421 65-88 (1983).

- 422 26: Dellino, P., Mele, D., Sulpizio, R., La Volpe, L. & Braia, G. A method for the calculation  
423 of the impact parameters of dilute pyroclastic density currents based on deposit particle  
424 characteristics. *J. Geophys. Res.* **113**, B07206 (2008).
- 425 27: Fisher, R. V., Schmincke, H.-U. & Van Bogaard, P. Origin and emplacement of a  
426 pyroclastic flow and surge unit at Laacher See, Germany. *J. Volcanol. Geotherm. Res.* **17**,  
427 375-392 (1983).
- 428 28: Cas, R. A. F. et al. The flow dynamics of an extremely large volume pyroclastic flow, the  
429 2.08-Ma Cerro Galán ignimbrite, NW Argentina, and comparison with other flow types. *Bull.*  
430 *Volcanol.* **73**, 1583-1609 (2011).
- 431 29: Middleton, G. V. Antidune cross-bedding in a large flume. *J. Sed. Petrol.* **35**, 922-927  
432 (1965).
- 433 30: Cartigny, M. J. B., Ventra, D., Postma, G. & Van Den Berg, J. H. Morphodynamics and  
434 sedimentary structures of bedforms under supercritical-flow conditions: New insights from  
435 flume experiments. *Sedimentology* **21**, 712-748 (2014).
- 436 31: Fisher, R. & Waters, A. Bed forms in Base-Surge deposits: Lunar implications. *Science*  
437 **26**, 1349-1352 (1969).
- 438 32: Fisher, R. & Waters, A. Base surge bed forms in maar volcanoes. *Am. J. Sci.* **268**, 157-  
439 180 (1970).
- 440 33: Waters, A. C. & Fisher, R. V. Base surges and their deposits: Capelinhos and Taal  
441 volcanoes. *J. Geophys. Res.* **76**, 5596-5614 (1971).
- 442 34: Crowe, B. & Fisher, R. Sedimentary structures in base-surge deposits with special  
443 reference to cross-bedding, ubehebe craters, death valley, California. *Bull. Geol. Soc. Am.* **84**,  
444 663-682 (1973).

- 445 35: Cole, P. & Scarpati, C. A facies interpretation of the eruption and emplacement  
446 mechanisms of the upper part of the Neapolitan Yellow Tuff, Campi Flegrei, southern Italy.  
447 *Bull. Volcanol.* **55**, 311-326 (1993).
- 448 36: Druitt, T. H. Emplacement of the 18 May 1980 lateral blast deposit ENE of Mount St.  
449 Helens, Washington. *Bull. Volcanol.* **54**, 554–572 (1992).
- 450 37: Gençalioglu-Kuşcu, C., Atilla, C., Cas, R. A. F. & Kuşcu, I. Base surge deposits, eruption  
451 history, and depositional processes of a wet phreatomagmatic volcano in Central Anatolia  
452 (Cora Maar). *J. Volcano. Geotherm. Res.* **159**, 198-209 (2007).
- 453 38: Brown, R. & Branney, M. Bypassing and diachronous deposition from density currents:  
454 Evidence from a giant regressive bed form in the Poris ignimbrite, Tenerife, Canary Islands.  
455 *Geology* **32**, 445-448 (2004).
- 456 39: Brand, B., Bendaña, S., Self, S. & Pollock, N. Topographic controls on pyroclastic  
457 density current dynamics: Insight from 18 May 1980 deposits at Mount St. Helens,  
458 Washington (USA). *J. Volcano. Geotherm. Res.* **321**, 1-17 (2016).
- 459 40: Roche, O., Gilbertson, M. A., Phillips, J. C. & Sparks, R. S. J. Experimental study of gas-  
460 fluidized granular flows with implications for pyroclastic flow emplacement. *J. Geophys.*  
461 *Res.-Sol. Ea.* **109**, B10201 (2004).
- 462 41: Girolami, L., Roche, O., Druitt, T. & Corpetti, T. Particle velocity fields and depositional  
463 processes in laboratory ash flows, with implications for the sedimentation of dense  
464 pyroclastic flows. *Bull. Volcanol.* **72**, 747-759 (2010).
- 465 42: Montserrat, S., Tamburrino, A., Roche, O. & Niño, Y. Pore fluid pressure diffusion in  
466 defluidizing granular columns. *J. Geophys. Res.* **117**, F02034 (2012).

- 467 43: Chédeville, C. & Roche, O. Autofluidization of pyroclastic flows propagating on rough  
468 substrates as shown by laboratory experiments. *J. Geophys. Res.-Sol. Ea.* **119**, 1764–1776  
469 (2014).
- 470 44: Rowley, P. J., Roche, O., Druitt, T. H. & Cas, R. Experimental study of dense pyroclastic  
471 density currents using sustained, gas-fluidized granular flows. *Bull. Volcanol.* **76**, 855 (2014).
- 472 45: Gueugneau, V., Kelfoun, K., Roche, O. & Chupin, L. Effects of pore pressure in  
473 pyroclastic flows: Numerical simulation and experimental validation. *Geophys. Res. Lett.* **44**,  
474 2194-2202 (2017).
- 475 46: Wilson, C. J. N. The role of fluidization in the emplacement of pyroclastic flows: An  
476 experimental approach. *J. Volcano. Geotherm. Res.* **8**, 231–249 (1980).
- 477 47: Giordano, G. The effect of paleotopography on lithic distribution and facies associations  
478 of small volume ignimbrites: the WTT Cupa (Roccamonfina volcano, Italy). *J. Volcanol.*  
479 *Geoth. Res.* **87**, 255-273 (1998).
- 480 48: Druitt, T. H., Avard, G., Bruni, G., Lettieri, P. & Maez, F. Gas retention in fine-grained  
481 pyroclastic flow materials at high temperatures. *Bull. Volcanol.* **69**, 881–901 (2007).
- 482 49: Hayashi, J. & Self, S. A comparison of pyroclastic flow and debris avalanche mobility. *J.*  
483 *Geophys. Res.* **97**, 9063-9071 (1992).
- 484 50: Calder, E. et al. Mobility of pyroclastic flows and surges at the Soufriere Hills Volcano,  
485 Montserrat. *Geophys. Res. Lett.* **26**, 534-540 (1999).
- 486 51: Lube, G. et al. Generation of air lubrication within pyroclastic density currents. *Nat.*  
487 *Geosci.* **12**, 381-386 (2019).

- 488 52: Smith, G., Williams, R., Rowley, P. & Parsons, D. Investigation of variable aeration of  
489 monodisperse mixtures: implications for pyroclastic density currents. *Bull. Volcanol.* **80**,67  
490 (2018).
- 491 53: Bareschino, P. et al. Fluidization and de-aeration of pyroclastic mixtures: the influence  
492 of fines content, polydispersity and shear flow. *J. Volcanol. Geotherm. Res.* **164**, 284–292  
493 (2007).
- 494 54: Iverson, R. M. & LaHusen, R. G. Friction in debris flows: Inferences from large-scale  
495 flume experiments. *Hydraulic engineering* 93, 1604-1609 (1993).
- 496 55: Iverson, R. M. The physic of debris flows. *Rev. Geophys.* 35, 245-296 (1997).
- 497 56: Savage, S. B. & Hutter, K. The motion of a finite mass of granular material down a rough  
498 incline. *J. Fluid Mech.* **199**, 177-215 (1989).
- 499 57: Bagnold, R. A. Experiments on a gravity-free dispersion of large solid spheres in a  
500 Newtonian fluid under shear. *Proc. R. Soc. London, Ser. A* **225**, 49-63 (1954).
- 501 58: Giordano, G. & Dobran, F. Computer simulations of the Tuscolano Artemisio's second  
502 pyroclastic flow unit (Alban Hills, Latium, Italy). *J. Volcanol. Geoth. Res.* **61**, 69-94 (1994).
- 503 59: Marra, F., Karner, D. B., Freda, C., Gaeta, M. & Renne, P. Large mafic eruptions at  
504 Alban Hills Volcanic District (Central Italy): Chronostratigraphy, petrography and eruptive  
505 behavior. *J. Volcanol. Geotherm. Res.* **179**, 217–232 (2009).
- 506 60: Giordano, G. et al. Stratigraphy, volcano tectonics and evolution of the Colli Albani  
507 volcanic field. In: Funicello, R., Giordano, G. (Eds.) *The Colli Albani Volcano Spec. Publ.*  
508 *IAVCEI* **3**, 43-98 (2010).

- 509 61: Trolese, M., Giordano, G., Cifelli, F., Winkler, A. & Mattei, M. Forced transport of  
510 thermal energy in magmatic and phreatomagmatic large volume ignimbrites: Paleomagnetic  
511 evidence from the Colli Albani volcano, Italy. *Earth. Planet. Sc. Lett.* **478**, 179-191 (2017).
- 512 62: Giordano, G. & Doronzo, D. M. Sedimentation and mobility of PDCs: a reappraisal of  
513 ignimbrites' aspect ratio. *Sci. Rep.* **7**, 1-7 (2017).
- 514 63: Conticelli, S. et al. (2010) Geochemistry, isotopes and mineral chemistry of the Colli  
515 Albani volcanic rocks: constraints on magma genesis and evolution. In: Funicello, R.,  
516 Giordano, G. (Eds.) *The Colli Albani Volcano, Spec. Publ. IAVCEI* **3**, 107-139 (2010).
- 517 64: Brand, B. & Clarke, A. An unusually energetic basaltic phreatomagmatic eruption: Using  
518 deposit characteristics to constrain dilute pyroclastic density current dynamics. *J. Volcanol.*  
519 *Geotherm. Res.* **243-244**, 81-90 (2012).
- 520 65: Rowley, P., MacLeod, N., Kuntz, M., Kaplan, A. Proximal bedding deposits related to  
521 pyroclastic flows of May 18, 1980, Mount St. Helens, Washington. *Bull. Geol. Soc. Am.* **96**,  
522 1373-1383 (1985).
- 523 66: R. V. Fisher & H.-U. Schmincke. *Pyroclastic Rocks* (Springer-Verlag, Berlin, 1984).
- 524 67: Boudet, J. F., Amarouchene, Y., Bonnier, B. & Kellay, H. The granular jump. *J. Fluid.*  
525 *Mech.* **572**, 413-431 (2007).
- 526 68: Faug, T. Depth-averaged analytic solutions for free-surface granular flows impacting  
527 rigid walls down inclines. *Phys. Rev. E* **92**, 062310 (2015).
- 528 69: Faug, T., Childs, P., Wyburn, E. & Einav, I. Standing jumps in shallow granular flows  
529 down smooth inclines. *Phys. Fluids.* **27**, 073304 (2015).

530 70: Douillet, G. et al. Pyroclastic dune bedforms: macroscale structures and lateral variations.  
531 Examples from the 2006 pyroclastic currents at Tungurahua (Ecuador). *Sedimentology*  
532 (2018).

533 71: Iverson, R. M. & Denlinger, R. P. Flow of variably fluidized granular masses across  
534 three-dimensional terrain: 1. Coulomb mixture theory. *J. Geophys. Res.* **106**, 537-552 (2001).

535 72: Geldart, D. Types of gas fluidization. *Powder Technol* **7**, 285–292 (1973).

536 73: Carrigy, M. A. Experiments on the angles of repose of granular materials. *Sedimentology*  
537 **14**, 147-158 (1970).

538 74: Rowley, P. J., Kokelaar, P., Menzies, M. & Waltham, D. Shear-derived mixing in dense  
539 granular flows. *J. Sediment. Res.* **81**, 874-884 (2011).

540 75: Fielding, C. R. Upper flow regime sheets, lenses and scour fills: Extending the range of  
541 architectural elements for fluvial sediment bodies. *Sediment. Geol.* **190**, 227-240 (2006).

## 542 **ACKNOWLEDGEMENTS**

543 This work was carried out as part of a PhD project funded by a University of Hull PhD  
544 scholarship in the Catastrophic Flows Research Cluster. Experiments were performed in the  
545 Geohazards Lab at the University of Portsmouth, using equipment funded by a British  
546 Society for Geomorphology Early Career Researcher Grant held by PR. DP was supported  
547 through funding from the European Research Council (ERC) under the European Union's  
548 Horizon 2020 Research and Innovation Programme (Grant Agreement no. 72955). GG,  
549 MT, and AS gratefully acknowledge The Grant of Excellence Departments, MIUR-Italy.  
550 We would like to thank Benjamin Andrews and Guilhem Douillet whose comments  
551 substantially improved this manuscript.

552



**553 AUTHOR CONTRIBUTIONS**

554 GS carried out experimental work and drafted the manuscript. GS, PR, GG, MT, and AS  
555 carried out fieldwork. GS, PR, and RW analysed experimental data. GS, PR, RW, GG, MT,  
556 AS, and DP discussed results and edited/commented on the manuscript. Characterisation of  
557 the experimental materials was led by SC.

**558 COMPETING INTERESTS**

559 The authors declare no competing interests.

560

561

562

563

564

565

566

567

568

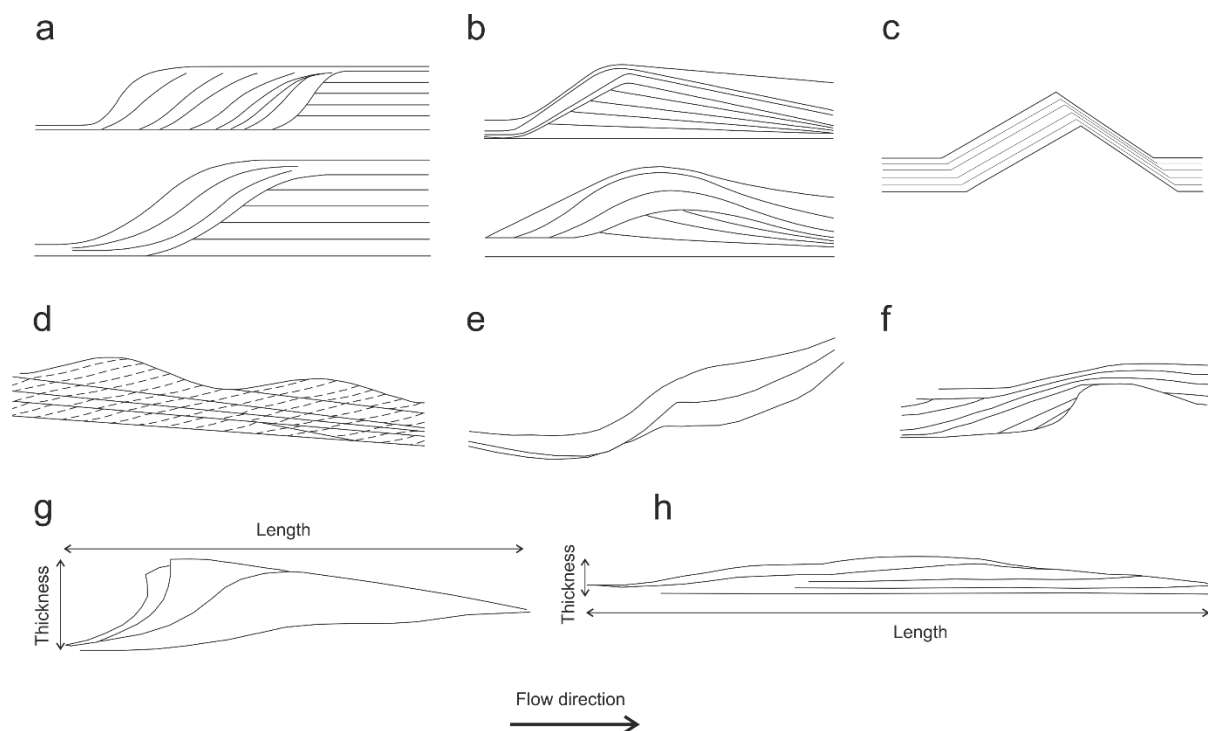
569

570

571

572

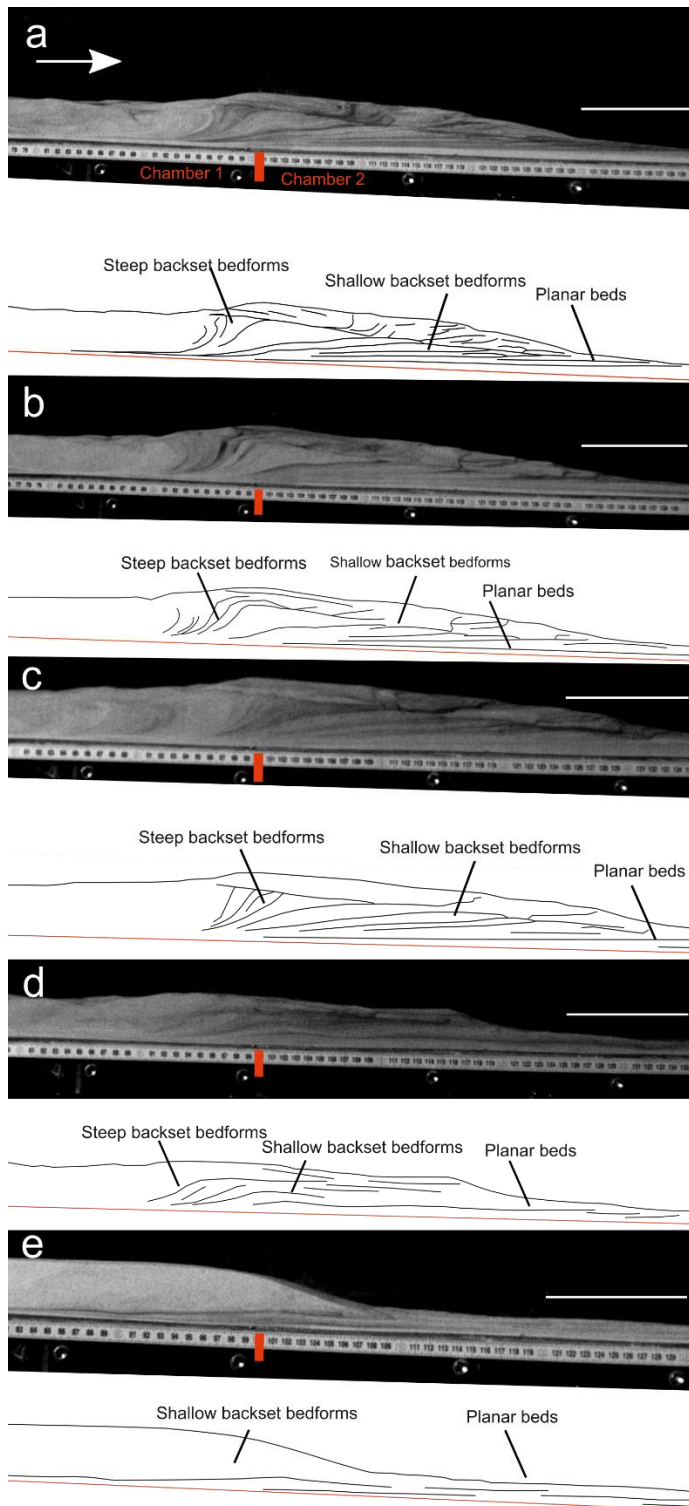
## 573 FIGURES &amp; CAPTIONS



574

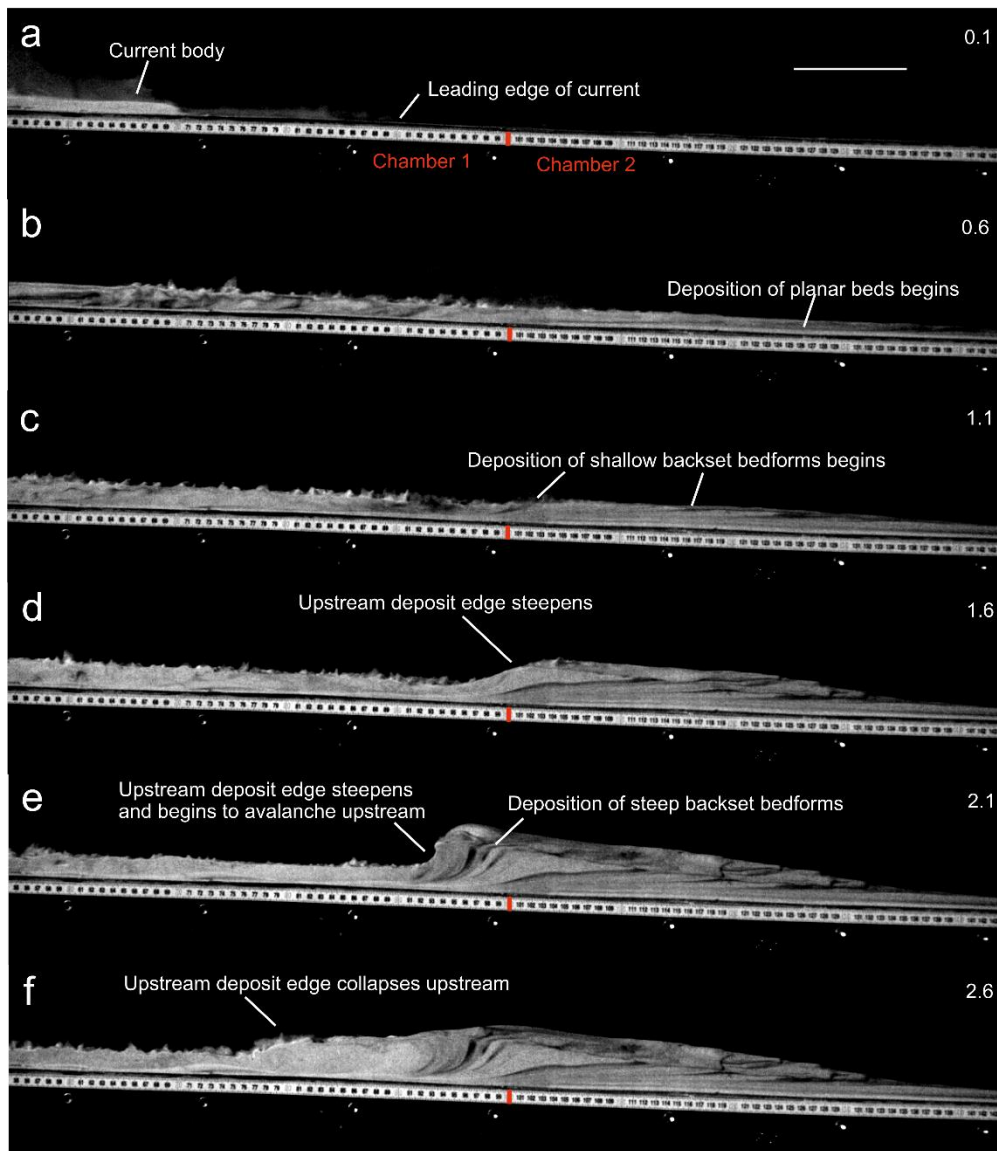
575 Fig. 1. Sketches of backset bedforms in PDC deposits. **a** Chute-and-pool structures in dilute  
 576 PDC deposits at Laacher See<sup>20</sup>. **b** Antidunes in dilute PDC deposits at Laacher See<sup>20</sup>. **c**  
 577 Regressive dune bedform<sup>22</sup>. **d** Stable antidunes<sup>30</sup>. **e** Regressive bedform from the Proximal  
 578 Bedded Deposits at Mt St Helens<sup>39</sup>. **f** Fluvial chute-and-pool structure<sup>75</sup>. **g** Steep backset  
 579 bedform as described in this paper, showing length and thickness definitions. **h** Shallow  
 580 backset bedform as described in this paper.

581



582

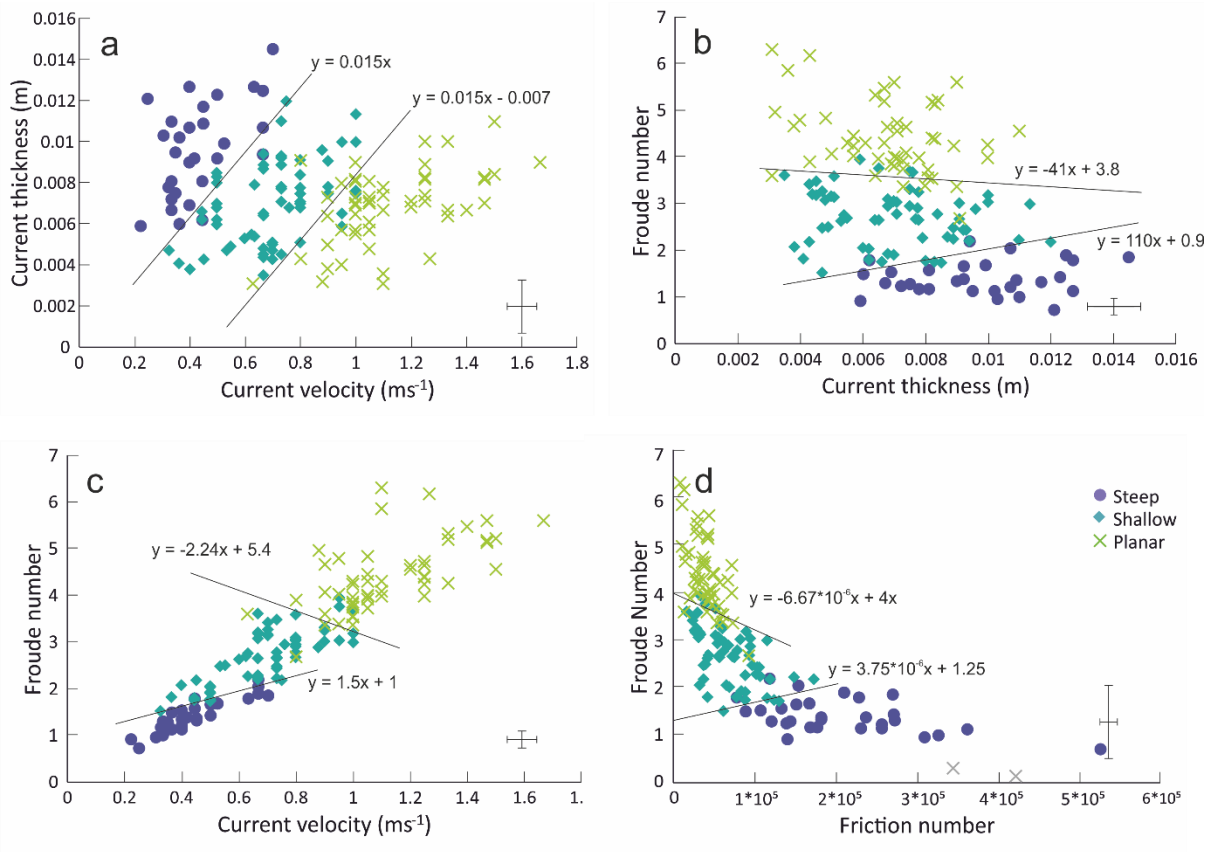
583 Fig. 2. Deposits from five separate experimental runs. Scale bar = 10 mm. **a, b, c** show584 backset bedforms deposited by currents passing above a chamber aerated at  $0.93 U_{mf}$  to one585 unaerated. **d** shows backset bedforms deposited by a current passing above a chamber aerated586 at  $0.93 U_{mf}$  to one aerated at  $0.66 U_{mf}$ . **e** shows backset bedforms deposited by a current587 passing above a chamber aerated at  $0.66 U_{mf}$  to one aerated at  $0.53 U_{mf}$ .



588

589 Fig. 3. Timelapse of an experimental granular current. Scale bar = 10 mm. Deposition of  
 590 backset bedforms is triggered by the current passing above a chamber aerated at  $0.93 U_{mf}$  to  
 591 one unaerated. See text for detailed description. Number in the top right of the frames is the  
 592 time in seconds since the current entered the first frame.

593

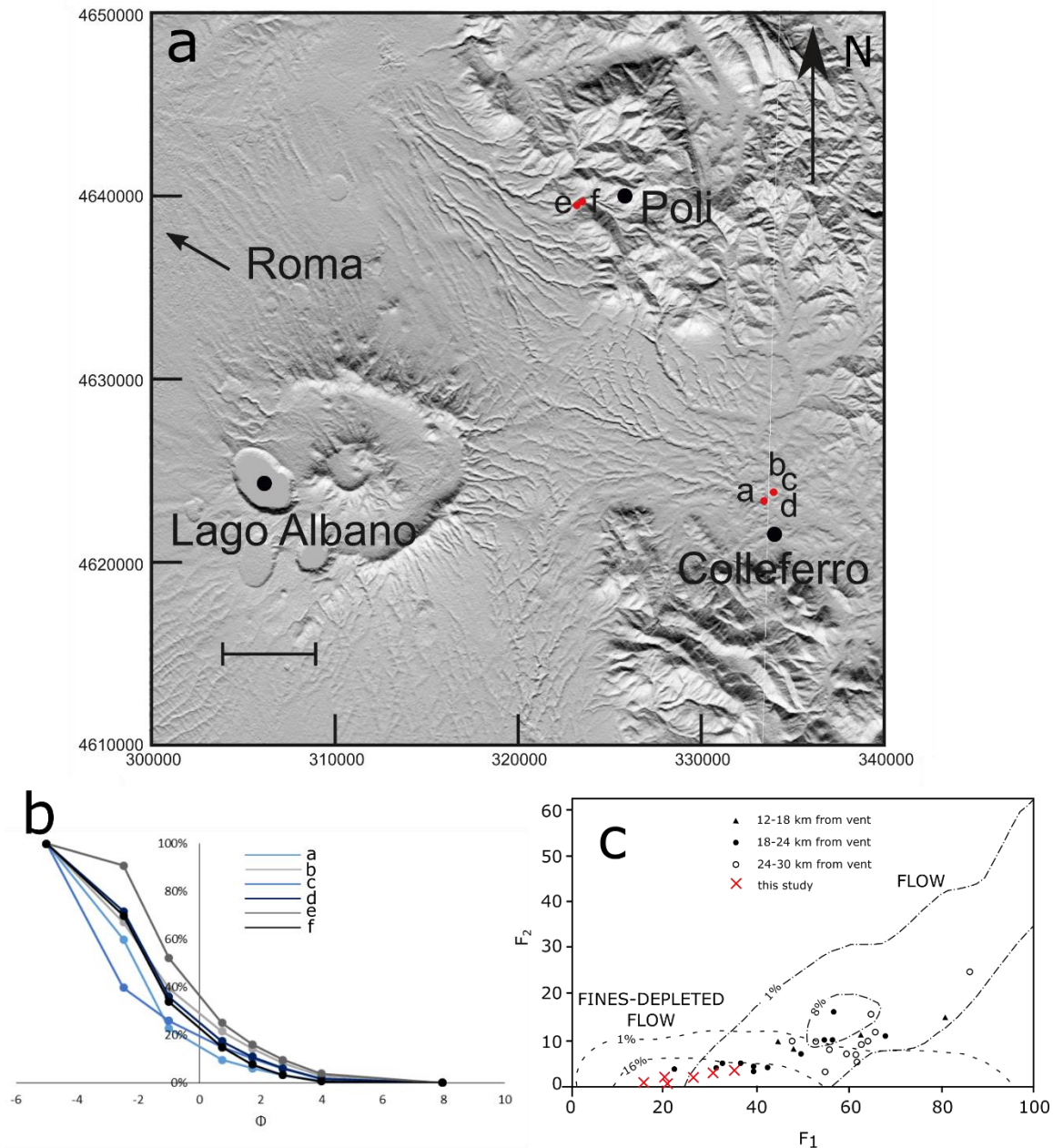


594

595 Fig. 4. Phase diagrams showing the current conditions which control backset bedform  
 596 formation, with plausible phase boundaries. **a** Velocity vs. thickness. **b** Thickness vs. Froude  
 597 number. **c** Velocity vs. Froude number. **d** Friction number vs. Froude number. Representative  
 598 ( $n = 20$ ) error bars are located in the bottom right of each image ( $\pm 2$  s.d.).

599

600



601

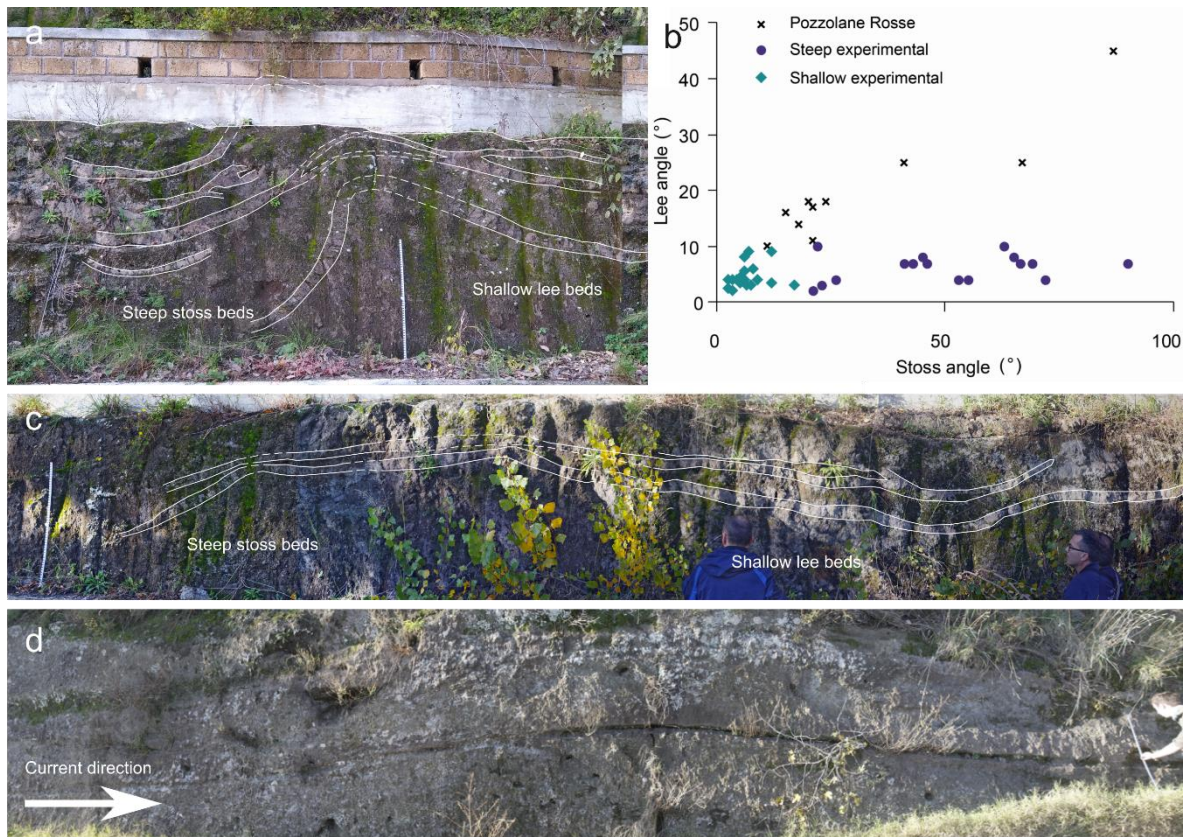
602 Fig. 5. a Map of Colli Albani volcano showing location of samples from the Pozzolane Rosse

603 ignimbrite. Scale bar = 5 km. Sample a is from the massive facies, sample b,c, and d from the

604 undulated bedding facies, and sample e and f from backset bedforms within this facies. b

605 Grain size distribution curves for samples from this study. Note the dominance of coarse

606 grains and paucity in the  $<63 \mu\text{m}$  ( $4 \phi$ ) fraction. The grain size data are given in607 Supplementary Table 2. c Plot of weight percentage finer than  $63 \mu\text{m}$  ( $F_2$ ) versus weight608 percentage finer than 1 mm ( $F_1$ ), after Walker<sup>25</sup>. Black symbols are PR ignimbrite samples609 from Giordano and Dobran<sup>58</sup>, red crosses show the PR ignimbrite samples from this study.



610

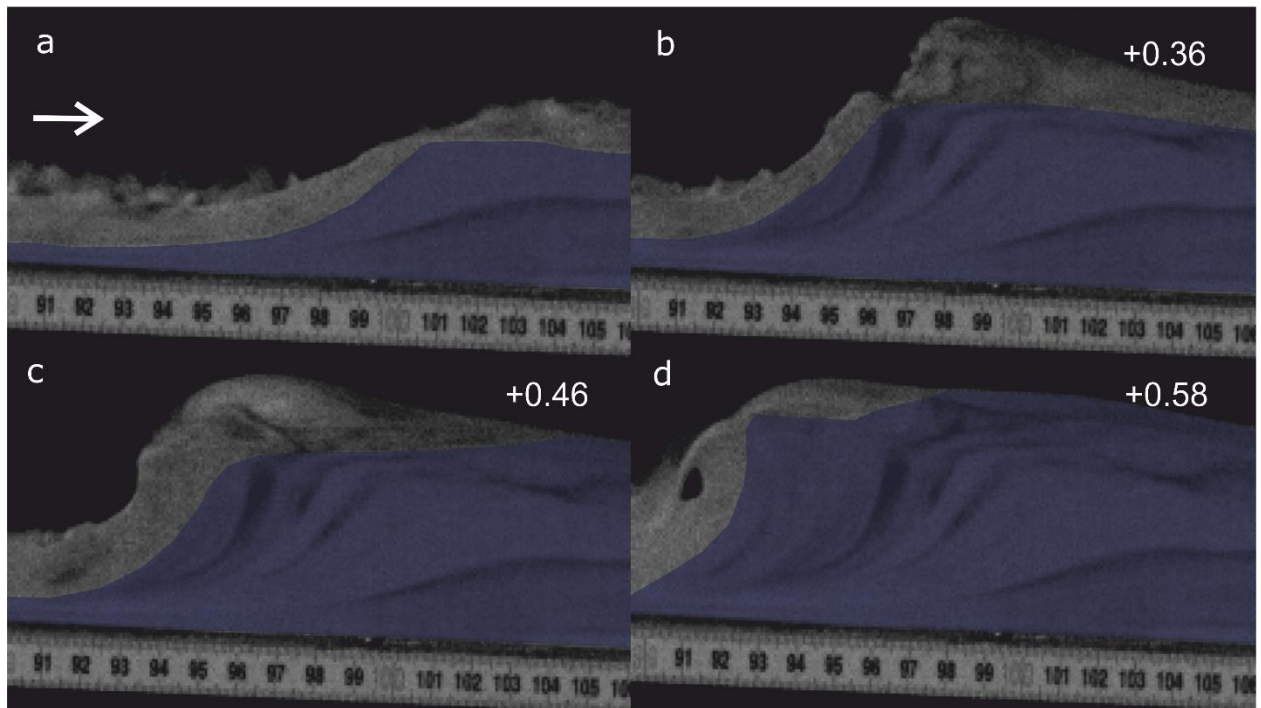
611 Fig. 6. Field photos and data of the Pozzolane Rosse ignimbrite erupted from Colli Albani,  
 612 Italy. The ruler is 1 m in length. Coordinates are for UTM 33T grid, using the WGS84  
 613 Datum. **a** steep stoss side backset bedform at 323348 4639535, c.f. Fig. 2a-c **b** stoss and lee  
 614 angles for PR and experimental backset bedforms. Several of these backset bedforms have  
 615 similar stoss angles to our experimental features, however the lee angles are much steeper. **c**  
 616 backset bedform directly upstream from **a**, c.f. Fig. 2d. **d** shallow bedform at 323037  
 617 4639270, thicker by ~15 cm over the stoss and crest compared to the lee.

618

619

620

621



622

623 Fig. 7. The formation and evolution of a granular bore. Numbers in the top right are seconds  
 624 passed since the first frame. Shaded area shows stationary deposit. Flow direction left to  
 625 right. **a** shows the initial formation of a steepening bump, with the incoming and outgoing  
 626 current both supercritical. **b** shows the upstream propagation and further steepening of the  
 627 bore, immediately after blocking of the outgoing current. **c** The bore propagates further  
 628 upstream, the front steepening to vertical. **d** The front of the bore collapses upstream by  
 629 avalanching.

630

631

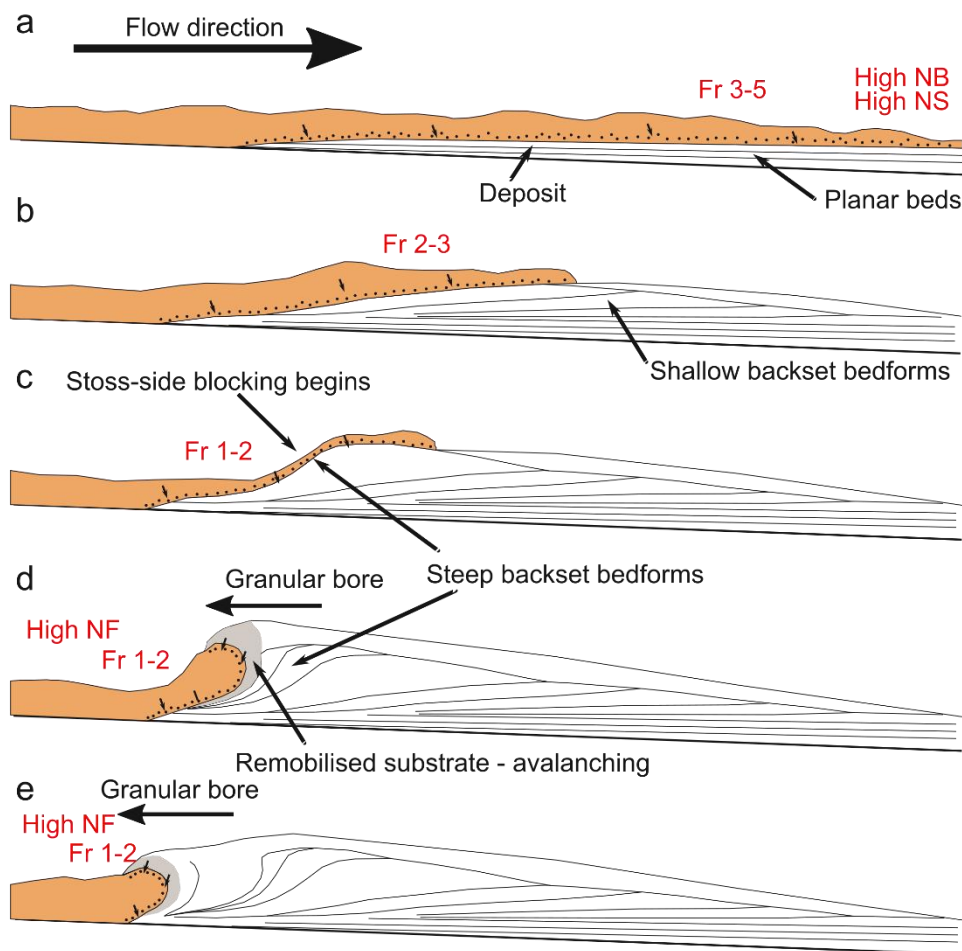
632

633

634

635





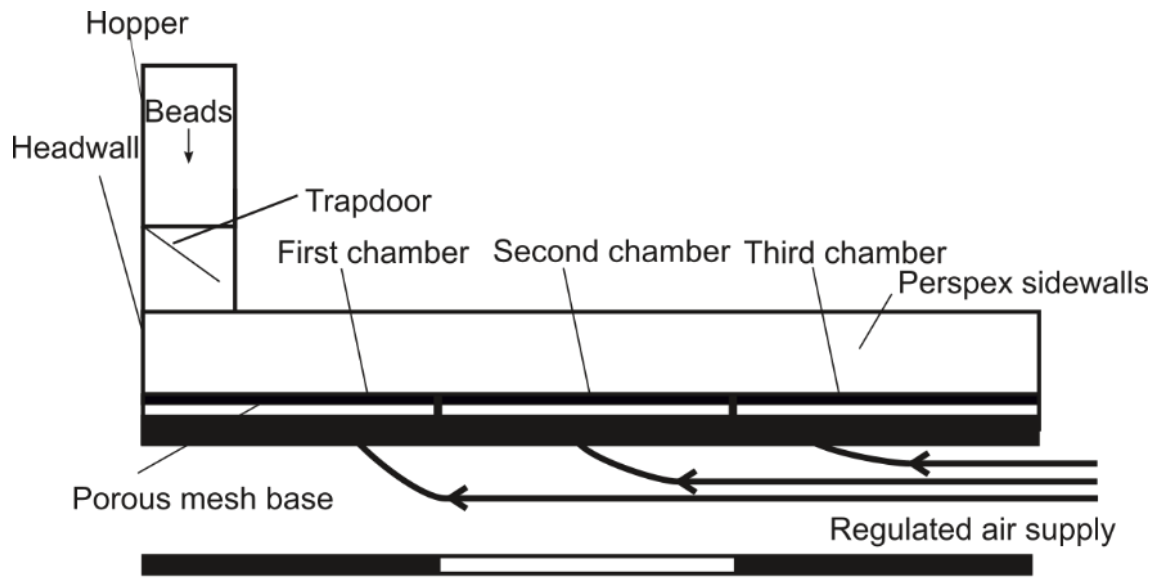
636

637 Fig. 8. Schematic showing how different backset bedforms could be deposited by a PDC.

638 Flow properties in red (Fr,  $N_S$ ,  $N_B$ ,  $N_F$ ) refer to the Froude, Savage, Bagnold, and Friction

639 Numbers respectively. See text for detailed description.

640



641

642 Fig. 9. A longitudinal section view of the experimental flume. Scale bar = 3 m.